Exploration of porphyry copper deposits within the municipality of Utuado using Operational Land Imager (OLI) sensor data and remote sensing methods

Elmer M. González Carrasquillo

elmer.gonzalez2@upr.edu

Department of Geology, University of Puerto Rico Mayaguez, P.O. Box 9012, Puerto Rico 00681

Abstract: Puerto Rico is a tropical island abundant in mineral resources ripe in commercial potential. Extensive mineral exploration was conducted in the past, yet modern laws placed since 1972 have prohibited further prospecting to be made. New methods have been developed; however, vegetation remains a major factor that could hinder any possible advances in future mineral exploration. The aim of this study is to apply remote sensing techniques for their possible viability in locating the porphyry copper deposits found at the southern margin of the Utuado batholith via changes in the spectral signal of the vegetation. A comparison was also made to areas that yield no known deposits and between the dates 2023 and 2017. ENVI 5.6.3 was used to conduct this research by applying various tools available in the program, such as NDVI, FCC, BR, PCA, and MNF, and Layer Stacking. Overall, the MNF and final composite images supported possible evidence of the possible detection of these deposit types in the area. These results are not completely conclusive as high vegetation and high noise to data ratio hinder any remote sensing techniques from properly detecting mineral deposits in Puerto Rico. Other methods such as fieldwork and alternative mineral methods, such as hydrogeochemical prospecting, are recommended for any potential mineral explorations conducted in the future.

Keywords: Mineral Exploration, Porphyry Copper, Remote Sensing, OLI/TIRS, NDVI, PCA, MNF

INTRODUCTION

Puerto Rico has been known to have abundant mineral resources that are ripe in commercial potential (**Figure 1**). The geology of the island consists of volcanic, volcaniclastic, and sedimentary rocks that date between the Late Jurassic to the Early Tertiary periods (Weaver, 1992). These types of rocks are found within Puerto Rico's major plutonic formations such as the Utuado and San Lorenzo batholiths, located at the center and eastern regions of the island, respectively. Most of the mineral deposits of Puerto Rico are found along these formations and follow the trend of the major fault zones that intersect the island, namely the Northern Puerto Rico Fault Zone (NPRFZ) and the Southern Puerto Rico Fault Zone (SPRFZ).

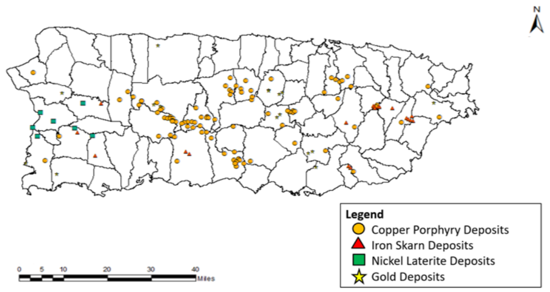

Figure 1. Map of all known major deposit types in Puerto Rico. Data from Mineral Resources Data System (MRDS), from U.S. possessions and associated areas (https://mrdata.usgs.gov/mrds/geo-inventory.php). Adapted from Cox and Briggs, 1973.

In its nearly 530-year-old history, the island's resources have been exploited by many foreign groups such as the Spanish conquistadors of the 16th century and American mining companies amidst the 20th century. Large mining operations took place within different mineral rich sectors of the island, where massive quantities of ore were extracted (Knoerr, 1952). As a result of this extensive mineral exploration, all known major deposits have been mapped since 1973 (MRDS, 2021). In modern times, new laws (i.e., the Mining Law of 1972) established by the Department of Natural and Environmental Resources (DRNA) have greatly limited mineral prospecting and further exploitation (Gelabert, 2011). Two factors have greatly influenced the placing of these laws: environmental concerns and increasing population levels (Gelabert, 2011). New methods have been developed to bypass these restrictions via a more indirect approach. Remote sensing techniques may prove to be useful in this endeavor as their impact on the environment is negligible. However, extensive vegetation covers most of the island, making any potential mineral exploration— albeit direct or indirect— difficult to conduct.

The focus of this project will be on porphyry copper deposits found within the southwestern region of the Utuado municipality. Compared to other mineral deposits such as nickel laterite and iron skarn, the porphyry copper deposits at the southern margin of the Utuado batholith (Miller, et. al., 1982) have been the site of extensive studies. The discovery of the Sapo Alegre outcrop in 1957 (Cox, et. al., 1975), followed by the subsequent discovery of the nearby deposits of Piedra Hueca and Cala Abajo in the years afterwards (Cox, et. al., 1975) drew the attention of various American mining companies to the area. During this period of mineral exploration, two major deposits of economic interest were found. Among these major deposits was the Río Tanamá deposit nestled at the southern margin of the Utuado batholith (Miller, et. al. 1982). The Río Tanamá deposit is composed of two ores that have no evident textural or compositional features, other than degree alteration and mineralization (Weaver, 1992). Magmatic intrusion is inferred to have occurred according to drill studies conducted on its porphyry stocks with its plutonic and metavolcanic rocks being intensely fractured, altered, and mineralized (Weaver, 1992). The main minerals found in this deposit are pyrite, chalcopyrite, and molybdenite, which are part of the hypogene sulfide minerals group (Miller, et. al., 1982; MRDS, 2021).

The main objectives of this project were: (1) to study the possible changes in vegetation signal between southwestern and northeastern Utuado, which are areas known to bare and not bare porphyry copper deposits, respectively, (2) to compare the sensor data of the area of interest between the years 2023 and 2017 for any possible differences in the spectral data, and (3) to test the viability of remote sensing techniques for the localization of future deposits of interest.

MATERIALS AND METHODS

Area of Study

Originally, this project was to compare the Tanamá deposit to another site where no known porphyry copper deposits have been found. The scope had expanded to include the larger region surrounding the Tanamá deposit as the southwestern and northeastern regions of Utuado are distinct geologically (Weaver, 1992). The southwestern region, where the Tanamá deposit is located, yields the formations of porphyry copper that are present within the southern margin of the Utuado batholith (Learned, et. al., 1982). Like most regions in Puerto Rico, this area is also heavily vegetated, which makes any potential mineral exploration difficult to conduct. However, as seen in **Figure 2**, this area was also affected by Hurricane María, which caused the vegetation density to heavily diminish.

Figure 2. True color image of area of study pertaining to OLI/TIRS sensor. Above: 2023. Below: 2017. Blue star is indicative of the Tanamá deposit.

Data Acquisition

Operational Land Imager (OLI)/Thermal Infrared Sensor (TIRS) is part of the latest Landsat 8/9 iteration. This pushbroom sensor has 11 bands with a spatial resolution of 30 m and a spectral range between 0.43 and 12.51 µm. OLI/TIRS also has the capacity of viewing images up to 15 m and 100 m for both panchromatic and thermal parameters, respectively. Other key features for this sensor include a temporal resolution of 16 days, radiometric resolution of 12 bits, and the ability to be programmable.

Earth Explorer was utilized to provide images pertaining to Layer 1 OLI/TIRS sensors. These images were particularly selected as the raw bands yield more data that allow for more thorough calculations compared to the more processed bands provided in Layer 2. Two images of different dates— 2023 and 2017, respectively— were selected for data comparison within the target areas of study. This selection of images was made due to the latter having significant visual differences compared to the former. Because of the passing of Hurricane Maria in September 2017, there existed the possibility of this region having different spectral signals compared to the most recent image taken in 2023.

Image Processing

The methods employed for this project were principally adapted from the methods of Khosravi, et. al. (2022) combined with Takodjou Wambo, et. al. (2020) for the heavily vegetated landscape of Puerto Rico. These methods heavily use ENVI and the various tools the program offers, specifically NDVI, false color (FCC) images, band ratios (BR), principal component analysis (PCA), minimum noise fraction transform (MNF), and layer stacking.

ENVI 5.6.3 was used to develop the appropriate rasters for the various image analyses tools that were previously mentioned. Two raster subsets were created for both raw images derived from the OLI/TIRS sensor (**Figure 10**). With these rasters created, the NDVI was directly calculated, and a mask was prepared for the vegetation indices for both images. Similar to previous work made, the masking was done by modifying the options of the Raster Management toolbox with the minimum and the maximum of the data range set to 0 and 1, respectively. To better highlight the differences between the vegetation values, a reverse green/white linear color scale was added. The equation used for calculating the NDVI values for both images is shown below:

$$NDVI = \frac{NIR - Red}{NIR + Red}$$

For the development of FCC, the RGB bands were assigned to bands 5 (NIR), 3 (Green), and 4 (Red) to create a false color image within the two created rasters. Three band ratios were also developed following the methods of Takodjou Wambo, et. al. (2020) with the different band ratios equations pertaining to bands 2 (Blue), 4 (Red), 5 (NIR), 6 (SWIR 1), and 7 (SWIR 2) being used. The equation utilized to determine the band ratios is as follows:

$$Band\ Ratio = \frac{Band\ A}{Band\ B}$$

For both PCA and MNF, seven bands were used: principally the VNIR and SWIR bands. A covariance matrix would be employed to determine the PCA images within all seven bands for both subsets (L3Harris, 2023), whilst the algorithms in MNF would separate the noise from the data to clear up the previous images (L3Harris, 2023). Once the FCC, BR, PCA, and MNF images were developed for both dates, layer stacking was employed to merge all images and bands into a single composite image. The standard red band, MNF band 4, and PCA band 7 were utilized to create the final, clearer image. For all images that were developed, a north arrow and scale bar (in kilometers) were added; a color bar for the NDVI and band ratio images was also included.

RESULTS

Eighteen images were developed for the OLI/TIRS sensor pertaining to NDVI, FCC, BR, PCA, MNF, and the final composite image. For simplicity, both the 2023 and 2017 images for each method will be placed side-by-side and be considered as a single figure. All figures are organized in the above-mentioned order.

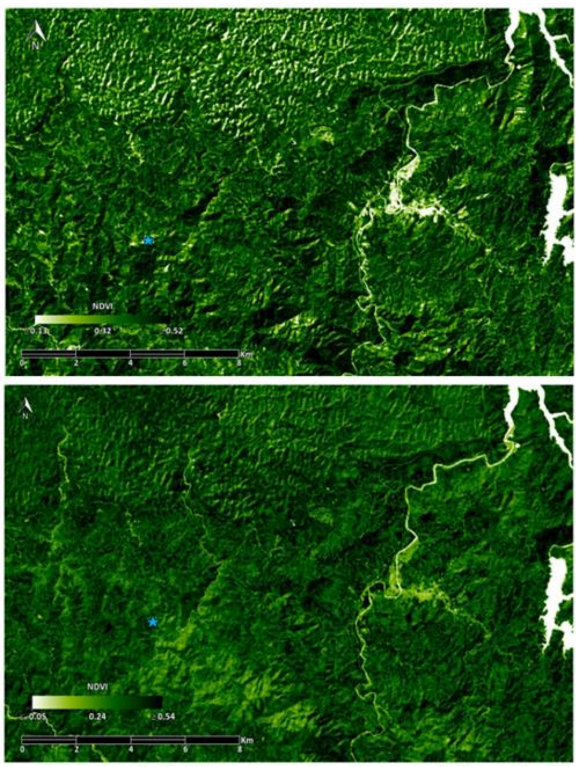

Figure 3. Normalized Difference Vegetation Index (NDVI) of area of study. True color digital image pertaining to OLI/TIRS sensor. Above: 2023. Below: 2017. Blue star is indicative of the Tanamá deposit.

The NDVI for both images yielded similar results, as seen in the color bar in **Figure 3**. The pixel data was slightly different, yet its results were expected. For the 2023 data, the highest vegetation value was 0.40 with the lowest value being 0.30. In contrast, the highest value for the 2017 data was 0.30 whilst the lowest value was 0.20. This difference in pixel size indicated that the vegetation was clearly affected by Hurricane Maria and had managed to steadily recuperate in the last six years.

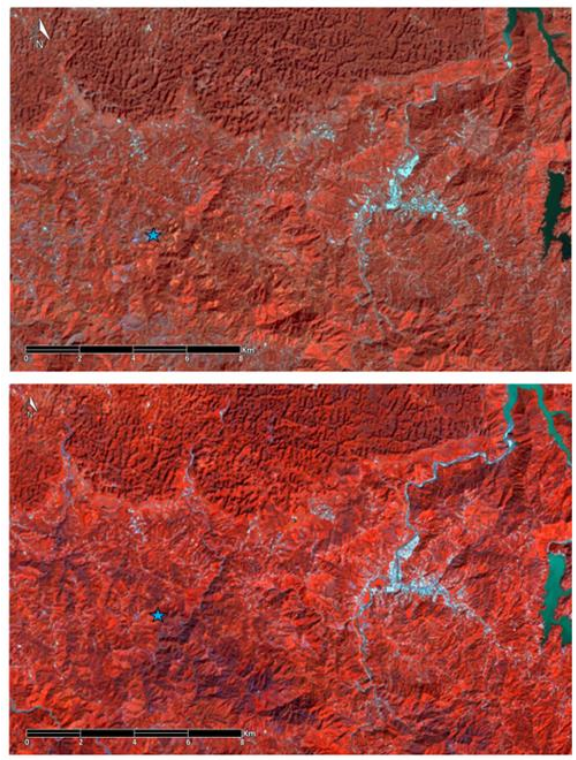

Figure 4. False color (FCC) of area of study pertaining to OLI/TIRS sensor. Above: 2023. Below: 2017. Blue star is indicative of the Tanamá deposit.

The FCC images for both dates revealed patterns that were not present in the initial true color images that were developed. As seen in **Figure 4**, some of the less vegetated areas in the southwest were more noticeable in comparison to the rest of the region. This was more apparent with the evident scarring in the 2017 image, which was characterized by a darker purple coloring. In contrast, urban areas were represented by pale white colors and vegetated areas by different shades of red.

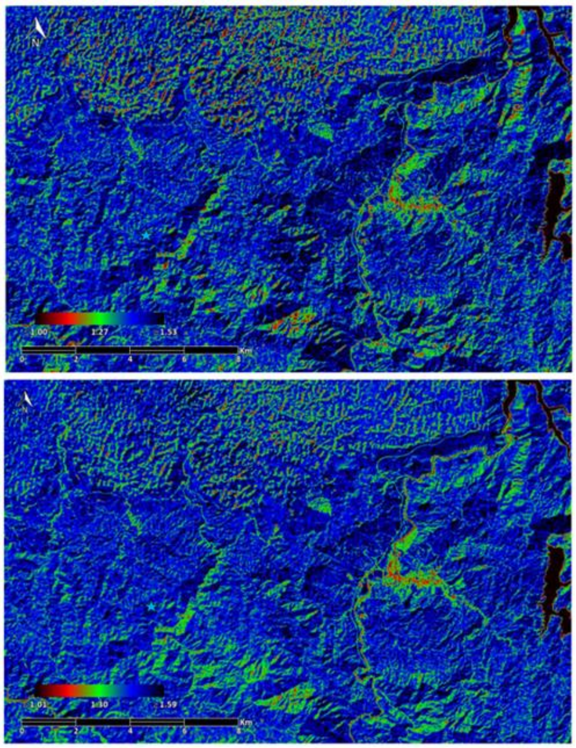

Figure 5. SWIR 1 and SWIR 2 band ratio of area of study pertaining to OLI/TIRS sensor. Above: 2023. Below: 2017. Blue star is indicative of the Tanamá deposit.

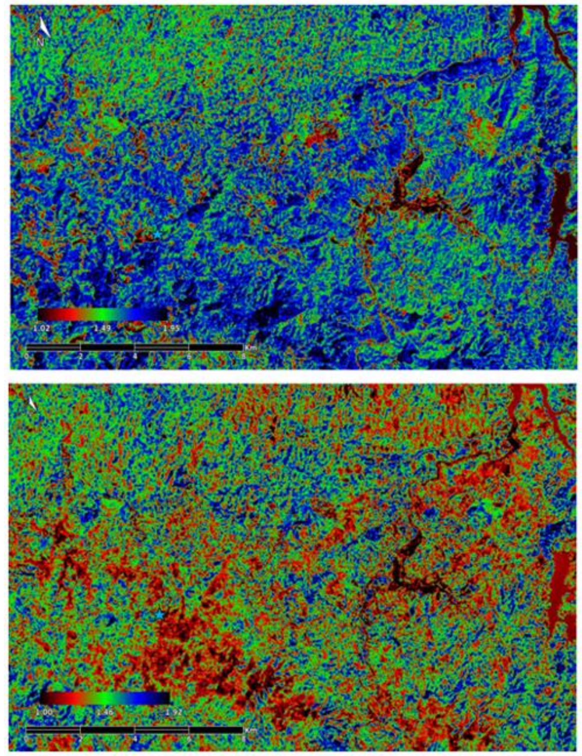

Figure 6. NIR and SWIR 1 band ratio of area of study pertaining to OLI/TIRS sensor. Above: 2023. Below: 2017. Blue star is indicative of the Tanamá deposit.

Although three BR combinations were made, the most definitive were those involving the NIR, SWIR 1, and SWIR 2 bands. The resulting images were more consistent amongst each other and were deemed the most representative of changes occurring in the vegetation. The selected BR images revealed interesting patterns regarding the vegetation of the region.

As seen in both **Figures 5** and **6**, blue represented vegetation, while green and red indicated that vegetation reduction had taken place with the former being more moderate whilst the latter more extreme. This relationship can be seen more prevalent in **Figure 6**, specifically in the 2017 image within the scarred region and some of the urban sectors close by. The combination of NIR and SWIR 1 bands highlighted more prominently the extent of Hurricane Maria's damage to the local environment.

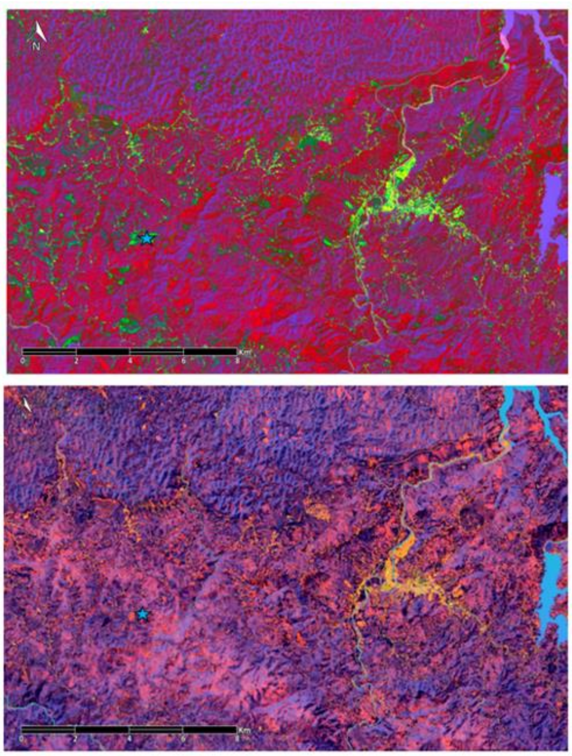

Figure 7. PCA of area of study pertaining to OLI/TIRS sensor. Above: 2023. Below: 2017. Blue star is indicative of the Tanamá deposit.

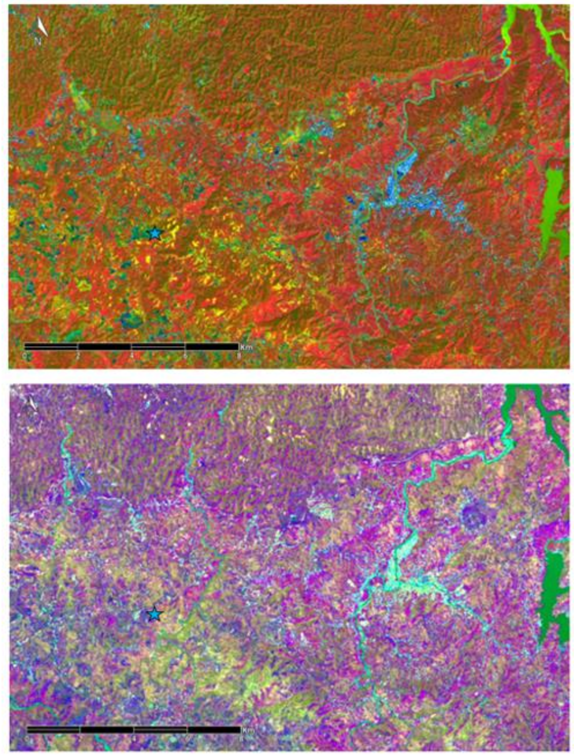

Figure 8. MNF of area of study pertaining to OLI/TIRS sensor. Above: 2023. Below: 2017. Blue star is indicative of the Tanamá deposit.

The images pertaining to PCA and MNF— seen in **Figures 7** and **8**— yielded more noticeable colors and patterns in comparison to the other images developed. This is evident with the 2017 images, which showed odd coloring in the previously mentioned affected area and a downward trend in accordance with the direction of the SPRFZ and the location of many known porphyry copper deposits. In general, the MNF images were clearer compared to the PCA images, which was expected. This is further supported by the eigenvalue plots and tabulated statistical results found in the **Appendix.**

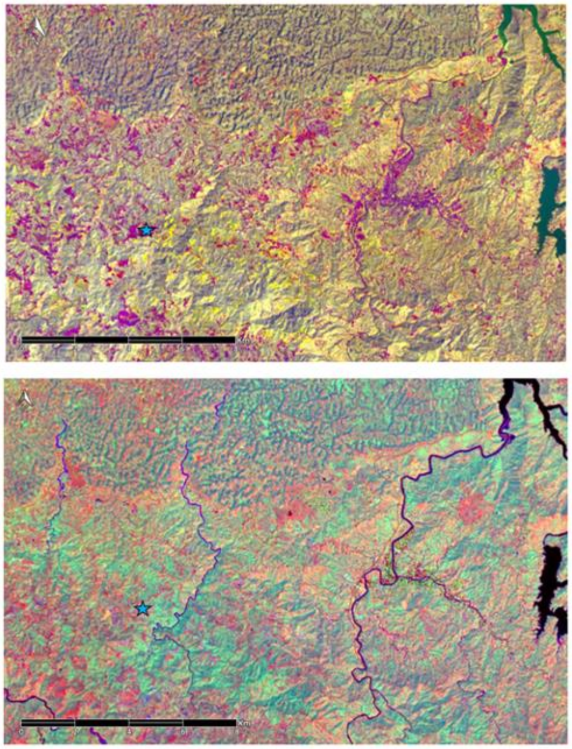

Figure 9. Final composite images of area of study pertaining to OLI/TIRS sensor. Above: 2023. Below: 2017. Blue star is indicative of the Tanamá deposit.

The final composite images for both dates, as seen in **Figure 9**, revealed similar trends in data. Though the color was not a defining feature compared to the previous PCA and MNF images, the downward trend can still be appreciated. Overall, these composite images support evidence that the vegetation signal might have yielded porphyry copper deposits in its vicinity.

DISCUSSION

With the NDVI, FCC, BR, PCA, MNF, and final composite images developed, sufficient data has been obtained to properly survey the target region. As expected, the 2023 images, which typically yielded the highest vegetation density as demonstrated by its NDVI, exhibited less evidence of porphyry copper deposits being detected within the vegetation's spectral signal. This is further supported by the high PCA eigenvalues plotted in **Figure 11**, which indicated that the amount of noise in contrast to data is much higher in order to properly survey the area for any mineral deposits via remote sensing methods. There are some outliers, however, such as the MNF and final composite images, but the high vegetation density and noise still clutter the overall data.

In comparison, the 2017 images exhibited more interesting trends in its data. Due to the more exposed landscape caused by the damage done during Hurricane Maria's passing, the scarred hillsides of this region of Utuado yielded much lower vegetation density. This impact in the environment in turn exhibited peculiar spectral phenomena in many of the developed images, specifically the NIR/SWIR 1 BR, PCA, MNF, and final composite images. It can be considered that the 2017 MNF image yielded the most evidence of porphyry copper deposits being detected within the vegetation's spectral, due to its odd green coloring and downward trend. This is also supported by the high MNF eigenvalues plotted in **Figure 12**, which contained higher values compared to the 2023 eigenvalue plot. The final composite images for both dates reveal the possibility of this change in the vegetation spectral data as possible, specifically in the 2017 image, yet not in the same magnitude as the 2017 MNF image discussed previously.

Despite the MNF and final composite images from 2017 yielding possible evidence of locating porphyry copper deposits via changes in the vegetation signal, these results are not completely conclusive. In retrospective, this further confirmed the previous notions that remote sensing techniques cannot properly detect these deposit types— nor possibly any mineral formation for that matter— in heavily vegetated regions due to high noise to data ratio and other external factors. In terms of future mineral exploration in Puerto Rico, these results do demonstrate that remote sensing techniques are not sufficient for this type of study in this region of the globe. For Puerto Rico's landscape, field work is recommended, along with alternative mineral exploration methods (such as hydrogeochemical prospecting) to properly survey the island for both known and unknown mineral deposit sites.

CONCLUSIONS

It is unclear if porphyry copper deposits were able to be properly identified within the vegetation signal in every developed image. Interesting trends can be appreciated within both the MNF and composite images with the 2017 data yielding the most direct possible evidence of this deposit type. However, the uncertainty of evidence provided by these analyses proves that remote sensing techniques are not ideal for mineral exploration in the heavy vegetated regions of Puerto Rico, even if the vegetation density has largely decreased. More data may be needed to validate any of these results; therefore, no conclusive evidence can be ascertained. Any future mineral exploration conducted in Puerto Rico should be done in a more direct manner, involving fieldwork and with alternative mineral exploration methods, such as hydrogeochemical prospecting.

RECOMMENDATIONS

For more thorough analysis, more time and resources are required. Possible additional resources include the use of spectral signal libraries and any physical data obtained during fieldwork. A larger time interval can also be adopted for future studies. Images pertaining to previous years, from other sensors, and from other planetary image databases, such as Copernicus and Planet Explorer, can be excellent sources for a similar project of this caliber and magnitude. Proper fieldwork can also be employed to confirm any possible findings within the developed images.

ACKNOWLEDGEMENTS

First, I would like to acknowledge Prof. Fernando Gilbes for assisting in this project, specifically in its direction and methodology. Secondly, I would also like to express gratitude to my colleagues in the class that helped with the project when any doubt emerged. Lastly, this project would never have bene possible if it had not been for the USGS to provide the databases that would serve as the primary source for the images that were selected.

WORKS CITED

Bishop, C. A., Liu, J. G., Mason, and P. J. 2011. Hyperspectral remote sensing for mineral exploration in Pulang, Yunnan Province, China. *Int. J. Remote Sens.* 32 (9): 2409 – 2426.

Campbell, J. B., and Wynne R. H. 2011. *Introduction to Remote Sensing*. The Guilford Press.

Cox, D. P. and Briggs, R. P. 1973. Metallogenic map of Puerto Rico: *Miscellaneous Geologic Investigations.* Map I-721.

Cox, D. P., Pérez González, I., and Nash, J. T. 1975. Geology, geochemistry, and fluid-inclusion petrography of the Sapo Alegre porphyry copper prospect and its metavolcanic wallrocks, west-central Puerto Rico. *J. Res. U.S. Geol. Surv.* 3: 313—327.

Fu, P., Zhang, W., Yang, K., Meng, F. 2020. A novel spectral analysis method for distinguishing heavy metal stress of maize due to copper and lead: RDA and EMD-PSD. *Ecotoxicol. Environ. Saf.* 206.

Gelabert, P. 2011. Minería en Puerto Rico: Recursos de Agua de Puerto Rico, https://web.archive.org/web/20210510003550/https://www.recursosaguapuertorico.com/Minería_en_Puerto_Rico_por_Pedro_Gelabert_PDF.pdf.

Khosravi, V., Shirazi, A., Shirazy, A., Hezarkhani, A., Beiranvand Pour, A. 2022. Hybrid Fuzzy-Analytic Hierarchy Process (AHP) Model for Porphyry Copper

Prospecting in Simorgh Area, Eastern Lut Block of Iran. *Min.* 2: 1—12.

Knoerr, A. W. 1952. Minnesota men open up rich Puerto Rico iron mine. *Eng. Min. J.* 153: 74—79.

L3Harris. 2023. Principal Component Analysis. https://www.l3harrisgeospatial.com/docs/principalcomponentanalysis.html.

L3Harris. 2023. Minimum Noise Fraction Transform. https://www.l3harrisgeospatial.com/docs/principalcomponentanalysis.html.

Miller, W. R., Ficklin, W. H., and Learned, R. E. 1982. Hydrogeochemical prospecting for porphyry copper deposits in the tropical-marine climate of Puerto Rico. *J. Geochem. Explor.* 16: 217 – 233.

Mineral Resources Data System (MRDS). 2021. On U.S. possessions and associated areas. https://mrdata.usgs.gov/mrds/geo-inventory.php.

Purkis, S., and Klemas, V. 2011. *Remote Sensing and Global Environmental Change*. Wiley-Blackwell.

Robb, L. 2005. *Introduction to Ore-Forming Processes (first edition), in Surficial and Supergene Ore-Forming Processes*. Oxford: Blackwell.

Takodjou Wambo, J. D., et al. 2020. Identifying high potential zones of gold mineralization in a sub-tropical region using Landsat-8 and ASTER remote sensing data: A case study of the Ngoura-Colomines goldfield, eastern Cameroon. *Ore Geol. Rev.* 122.

Vincent, R. K. 1997. *Fundamentals of Geological and Environmental Remote Sensing*. Prentice Hall.

Weaver, J. N. 1992. Mineral resource assessment of Puerto Rico: U.S. Geological Survey Open-File Report 92-567. https://pubs.usgs.gov/of/1992/0567/report.pdf.

APPENDIX

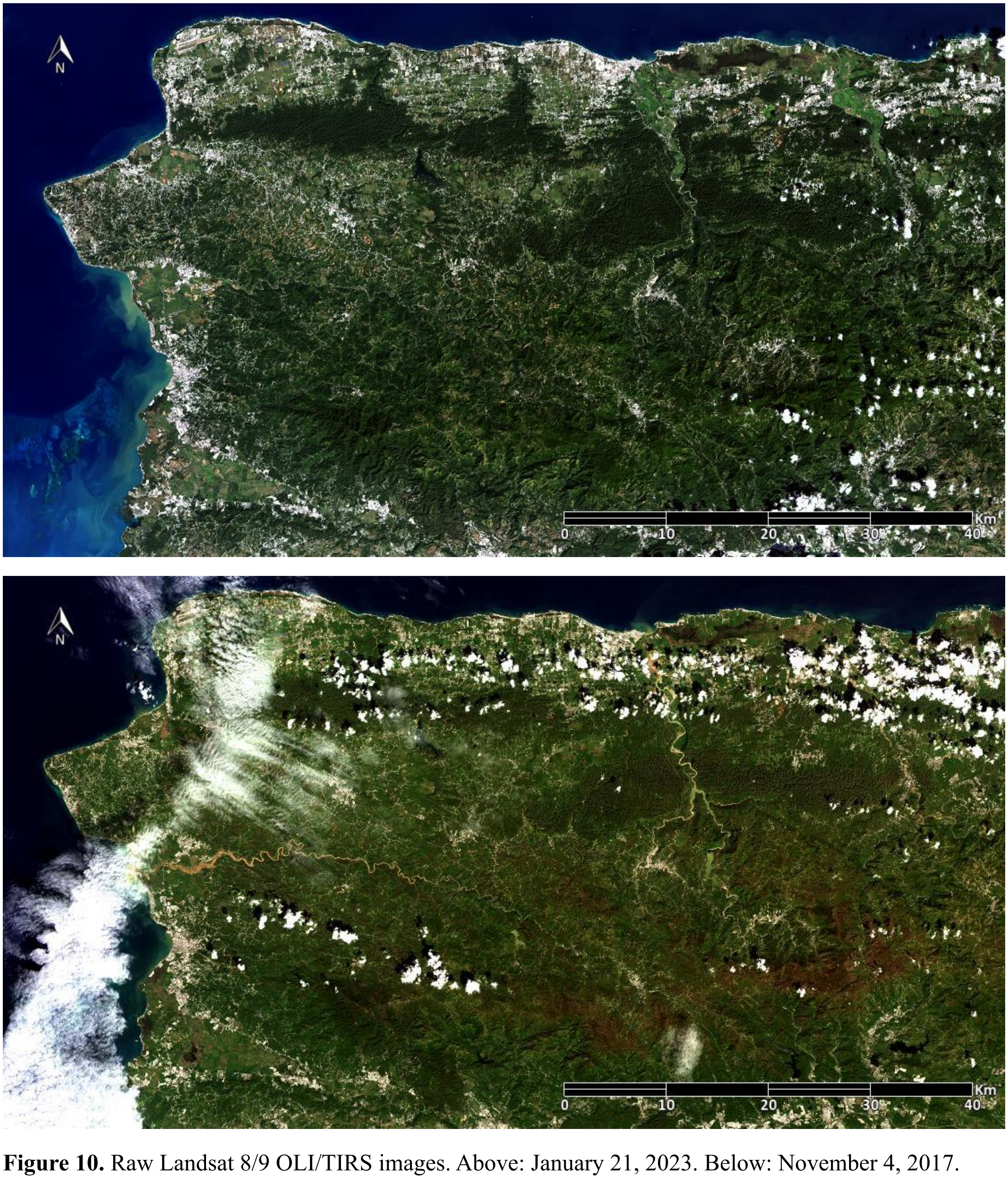

Figure 10. Raw Landsat 8/9 OLI/TIRS images. Above: January 21, 2023. Below: November 4, 2017.

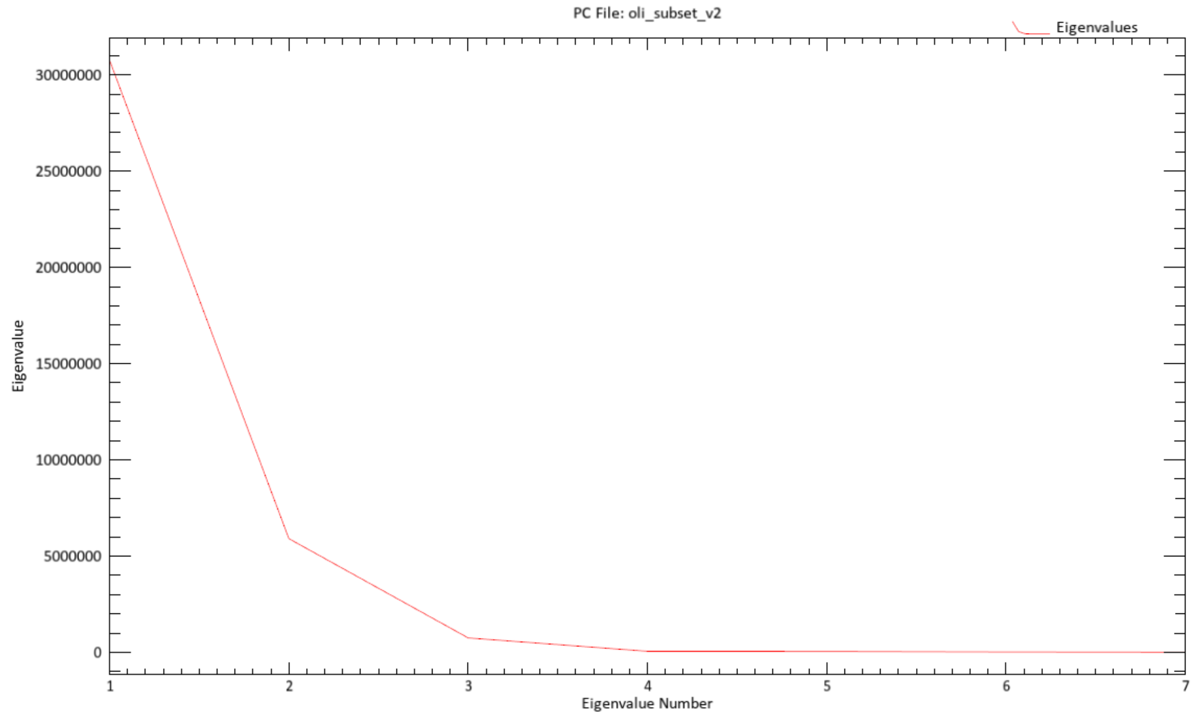

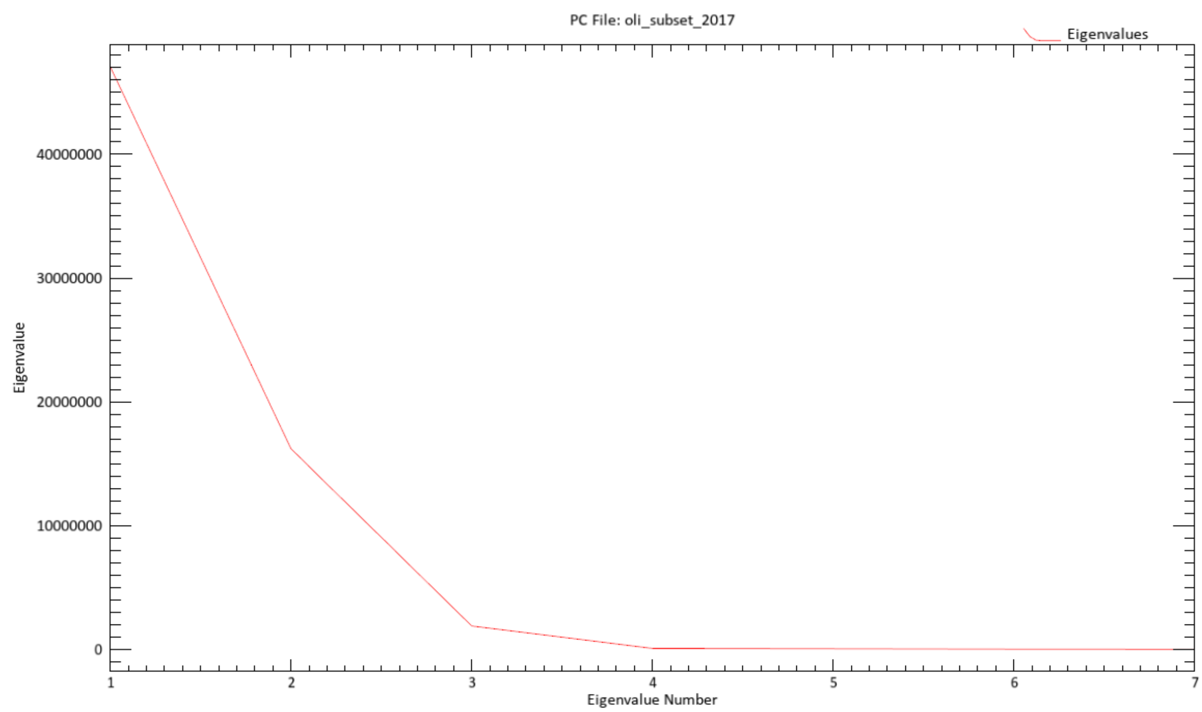

Figure 11. PCA eigenvalues plotted according to band number. Above: 2023. Below: 2017.

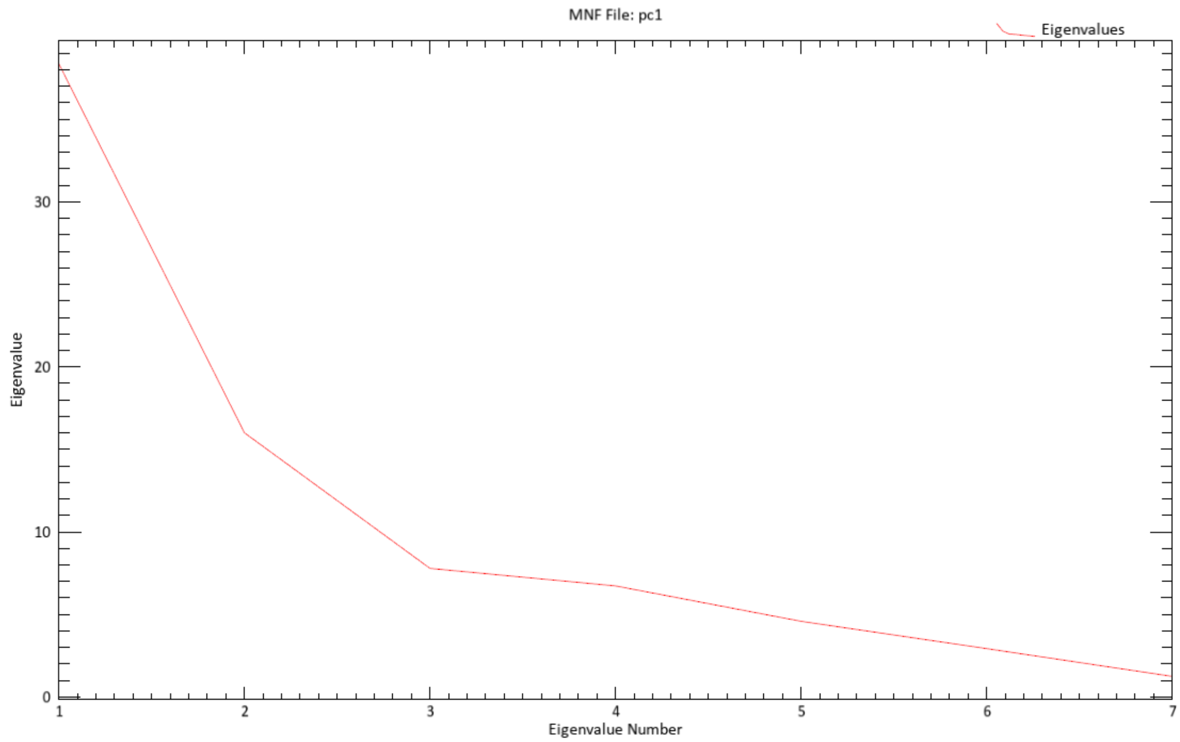

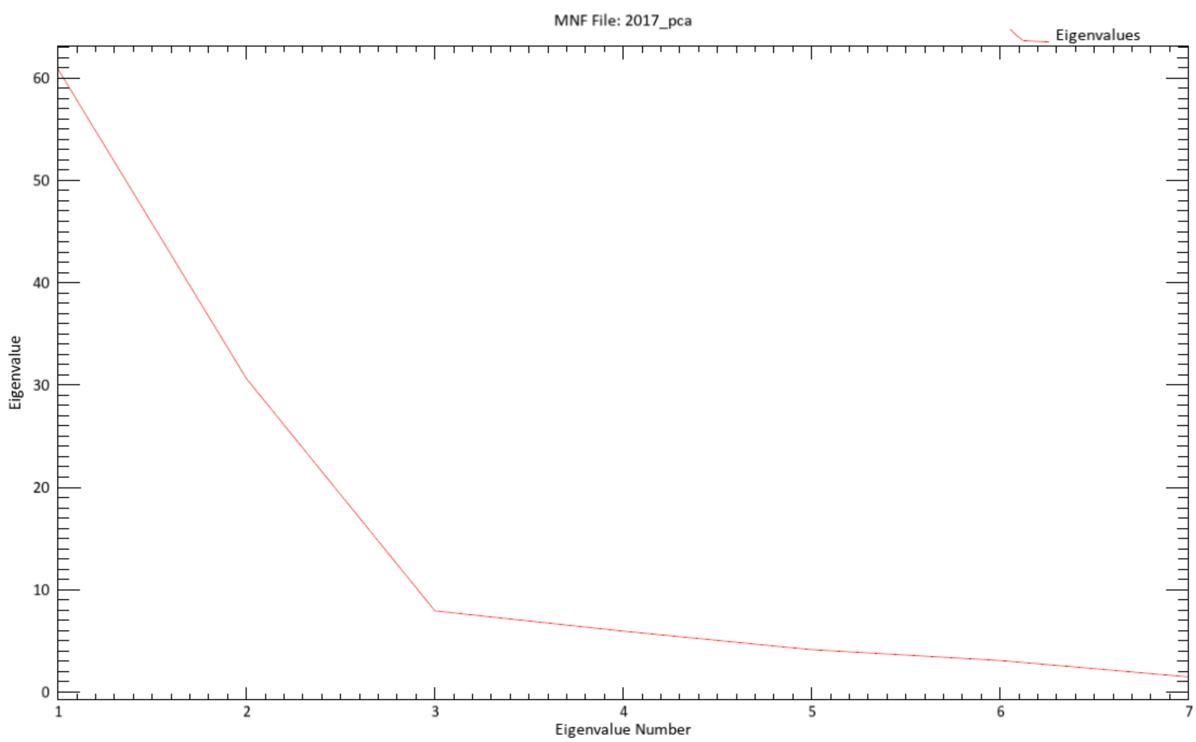

Figure 12. MNF eigenvalues plotted according to band number. Above: 2023. Below: 2017.

Table 1. Statistical results obtained from PCA for 2023 Data.

PC Bands	Eigenvalues	Eigenvalues (%)	Cumulative (%)
1	30753725.2	81.94777229	81.94777229
2	5905907.7	15.73714977	97.68492206
3	749143.41	1.996201539	99.6811236
4	53683.577	0.143047696	99.8241713
5	45521.595	0.121298909	99.94547021
6	17391.226	0.04634145	99.99181166
7	3072.9582	0.008188344	100

Table 2. Statistical results obtained from PCA for 2017 Data.

PC Bands	Eigenvalues	Eigenvalues (%)	Cumulative (%)
1	47076781.3	72.05797317	72.05797317
2	16207097.1	24.80735802	96.86533119
3	1892854.4	2.897293481	99.76262467
4	80586.127	0.12334898	99.88597365
5	51722.241	0.079168536	99.96514218
6	18441.662	0.02822769	99.99336987
7	4331.5826	0.006630128	100

Table 3. Statistical results obtained from MNF conversion for 2023 Data.

MNF Bands	Eigenvalues	Eigenvalues (%)	Cumulative (%)
1	38.368335	49.41201421	49.41201421
2	16.005878	20.61290048	70.02491469
3	7.7896164	10.03172632	80.05664101
4	6.7281654	8.664754525	88.72139554
5	4.5832758	5.902494569	94.62389011
6	2.9286182	3.771571639	98.39546175
7	1.2459209	1.604538253	100

Table 4. Statistical results obtained from MNF conversion for 2017 Data.

MNF Bands	**Eigenvalues**	**Eigenvalues (%)**	**Cumulative (%)**
1	60.868824	53.35345607	53.35345607
2	30.62861	26.84694875	80.20040482
3	7.934173	6.954554447	87.15495926
4	5.9505635	5.215857765	92.37081703
5	4.1412467	3.629934166	96.00075119
6	3.0835101	2.702794466	98.70354566
7	1.4790729	1.296454339	100